REECAP: Contrastive learning of retinal aging reveals genetic loci linking morphology to eye disease

Liubov Shilova[1,2,3,4], Daniel Sens[1,2,4], Ayshan Aliyeva[1,2], Shubham Chaudhary[1,2,4], Qiaohan Xu[7], Emmanuelle Salin[3], Johannes Schiefelbein[5], Ben Asani[5], Oana Veronica Amarie[6], Elida Schneltzer[6], Ayellet V. Segrè[7,8], Julia A. Schnabel[4,9,10], Na Cai[11], Bjoern M. Eskofier[1,3,12,@], Francesco Paolo Casale[1,2,4,@]

[1] Institute of AI for Health, Helmholtz Zentrum München – German Research Center for Environmental Health, Neuherberg, Germany
[2] Helmholtz Pioneer Campus, Helmholtz Zentrum München – German Research Center for Environmental Health, Neuherberg, Germany
[3] Friedrich-Alexander-Universität Erlangen-Nürnberg, Erlangen, Germany
[4] School of Computation, Information and Technology, Technical University of Munich, Garching, Germany
[5] Department of Ophthalmology, University Hospital, LMU Munich, Munich, Germany
[6] Institute of Experimental Genetics, Helmholtz Zentrum München, Munich, Germany
[7] Department of Ophthalmology, Massachusetts Eye and Ear, Harvard Medical School, Boston, MA, USA
[8] Broad Institute of Harvard and MIT, Cambridge, MA, USA
[9] Institute of Machine Learning in Biomedical Imaging, Helmholtz Zentrum München – German Research Center for Environmental Health, Neuherberg, Germany
[10] School of Biomedical Engineering and Imaging Sciences, King's College London, London, UK
[11] Department of Biosystems Science and Engineering, ETH Zürich, Basel, Switzerland
[12] Institute of AI in Medicine, LMU Klinikum, Munich, Germany

@ Correspondence to bjoern.eskofier@fau.de and francescopaolo.casale@helmholtz-munich.de

Abstract

Deep learning foundation models excel at disease prediction from medical images, yet their potential to bridge tissue morphology with the genetic architecture of disease remains underexplored. Here, we present REECAP (Representation learning for Eye Embedding Contrastive Age Phenotypes), a framework that fine-tunes the RETFound retinal foundation model using a contrastive objective guided by chronological age. Applied to 87,478 fundus images from 52,742 UK Biobank participants, REECAP aligns image representations along the aging axis, yielding multivariate ageing phenotypes for genome-wide association studies (GWAS). GWAS of REECAP embeddings identifies 178 loci, including 27 that colocalize with

risk loci of age-related eye diseases, 14 of which remained undetected by conventional disease-label GWAS. By enabling conditional image synthesis, REECAP further links genetic variation to interpretable anatomical changes. Benchmarking against alternative embedding models, we show that REECAP enhances both locus discovery and disease relevance of genetic associations, suggesting that aging-informed tissue embeddings represent a powerful intermediate phenotype to discover and interpret disease loci.

Introduction

Genome-wide association studies (GWAS) have mapped thousands of disease-associated loci, yet translating these signals into tissue-specific biological mechanisms remains a central challenge in human genetics.

One strategy to bridge this gap is to incorporate imaging-derived phenotypes as intermediate traits, which can increase both the statistical power and interpretability of genetic analyses[1–5]. Recent advances in deep learning–based phenotyping have extended this approach[6–13], yet most efforts remain task-specific and have not been systematically evaluated for their impact on genetic discovery.

Foundation models trained via self-supervised learning on large image datasets and fine-tuned for downstream tasks provide a powerful basis for studying tissue architecture and its links to disease, and are increasingly used for clinical prediction[14–20]. For example, in ophthalmology, the RETFound model achieves state-of-the-art performance in disease classification[20,21]. However, the application of foundation models to genetic discovery remains unexplored.

Here, we introduce REECAP (Representation learning for Eye Embedding Contrastive Age Phenotypes), a framework that fine-tunes the RETFound encoder using a contrastive objective guided by chronological age to capture representations enriched for age-related disease biology. Applied to fundus photographs from the UK Biobank (UKB), REECAP improves genetic discovery and interpretability compared to expert-defined and deep learning–based phenotypes, with enhanced colocalization to age-related eye diseases and links to retinal morphology.

Results

Contrastive fine-tuning of foundation models for tissue aging

To enhance the value of image-derived representations for disease genetics, we developed REECAP, a framework that fine-tunes vision foundation models via contrastive learning guided by chronological age, aligning the latent space along a continuous trajectory of retinal aging (**Fig. 1a**). Starting from RETFound[20,21], we applied REECAP to 87,478 high-quality

fundus images from 52,742 UKB participants and used the resulting embeddings as multivariate phenotypes in a GWAS (**Supplementary Fig. 1**).

To determine whether REECAP embeddings provide more informative signals for disease genetics than other image-derived phenotypes, we benchmarked them against alternative multivariate and univariate approaches (**Fig. 1b**). Beyond discovery, we assessed disease relevance through colocalization with major ocular disease GWAS from FinnGen (**Fig. 1c**), as well as polygenic risk prediction and pathway enrichment.

We next examined the biological processes and loci captured by REECAP (**Fig. 1d**). Specifically, we linked both known and novel disease loci discovered through REECAP to morphological changes in the eye using conditional image generation[12], producing synthetic fundus images conditional on REECAP embeddings, and to functional evidence from mouse knockout databases.

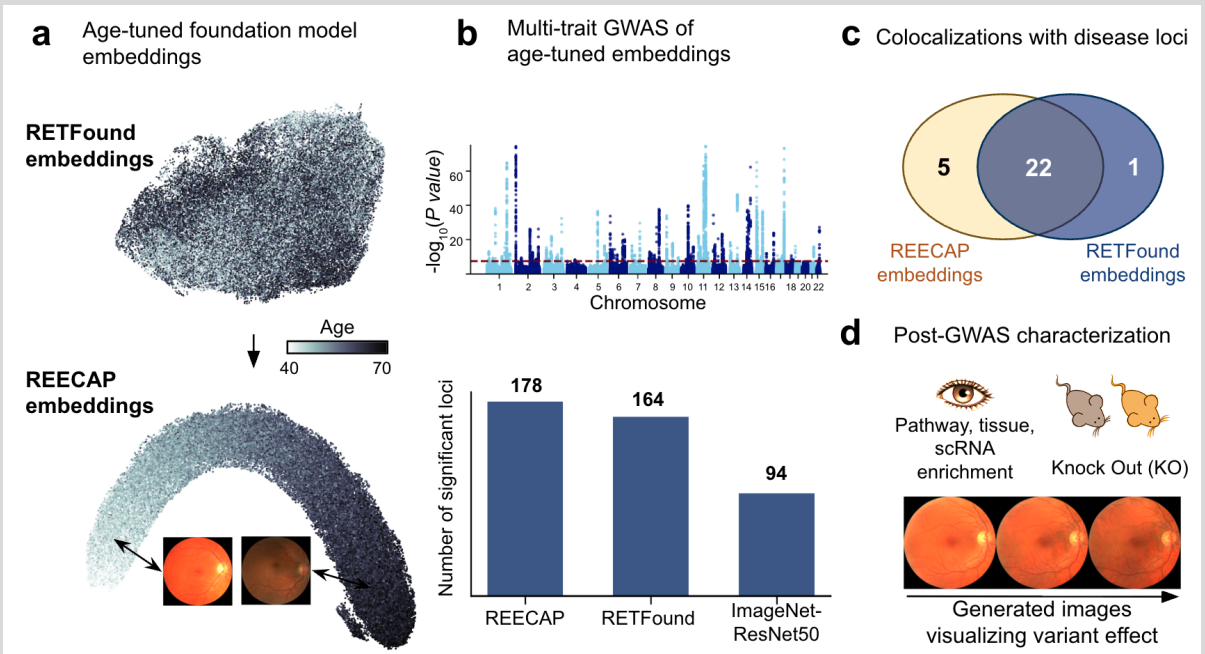

Figure 1 | Overview of the REECAP framework. (**a**) UMAP projection of fundus embeddings from RETFound (top) and REECAP (bottom). Contrastive fine-tuning on chronological age aligns the latent space along a continuous retinal aging axis, illustrated by example images from opposite extremes. (**b**) Multi-trait GWAS of REECAP embeddings identifies more genome-wide significant loci than baseline models. Top: Manhattan plot of REECAP associations. Bottom: number of loci detected by REECAP, RETFound, and ResNet50 (ImageNet-pretrained). (**c**) Disease relevance of REECAP loci. Venn diagram of colocalizations with ocular disease loci from FinnGen using REECAP versus RETFound embeddings. (**d**) Downstream characterization of REECAP loci, including pathway, tissue, and cell-type enrichment; conditional image synthesis of retinal morphology; and overlap with in vivo mouse knockout data.

Age-tuned embeddings capture biologically relevant retinal features

To capture eye features aligned with aging, we fine-tuned the RETFound encoder using a contrastive objective based on chronological age[22], which encourages representations of patients with similar ages to be closer than those of patients with larger age differences, effectively organizing the latent space along a continuous age trajectory. We applied this training to 87,478 high-quality fundus images from 52,742 UKB participants (**Methods**). The resulting REECAP representations substantially improved age prediction by linear probing (mean absolute error [MAE] = 2.86 ± 0.007 years), compared with the original RETFound representations (MAE = 3.40 ± 0.01 years; $P < 3\times10^{-7}$; **Fig. 2a**, **Methods**). REECAP also outperformed conventional supervised regression-based fine-tuning (MAE = 2.86 ± 0.007 versus 3.03 ± 0.003 years; $P < 5\times10^{-9}$; **Methods**); **Supplementary Fig. 2**), consistent with prior work showing superior performance of contrastive objectives over standard regression losses[22].

We next assessed the clinical relevance of REECAP by predicting five-year risk for major ocular diseases. REECAP embeddings improved risk prediction for glaucoma, retinal disorders (including age-related macular degeneration, AMD), and refraction disorders compared to untuned embeddings (Bonferroni-adjusted $P < 0.05$; **Fig. 2b–d**, **Methods**). Across all five conditions, REECAP performed as well as or better than both untuned RETFound and baseline models based on demographic variables (**Methods**).

To evaluate whether REECAP embeddings capture specific morphological features linked to aging and pathology, we leveraged a conditional generative framework to visualize patterns associated with age and future diagnosis. Specifically, we trained generative adversarial networks to generate synthetic images conditional on REECAP embeddings, using interpolation to visualize fundus changes across gradients of age and five-year disease risk (**Methods**, **Supplementary Fig. 3-7**)[12]. The resulting synthetic images were reviewed by two ophthalmologists, who confirmed distinct, clinically relevant patterns along each phenotypic axis. For aging, reconstructions showed progressive vessel narrowing and reduced image contrast, consistent with healthy fundus aging[23–25] (**Fig. 2c**, **Supplementary Fig. 3**). For retinal disorders, higher risk was associated with a slightly less pigmented fundus (**Fig. 2d**), consistent with early hypopigmentation of the retinal pigment epithelium—a known prognostic marker for progression to late AMD[26]—with individual samples additionally showing peripheral atrophy, pale optic discs, and altered foveal reflexes (**Supplementary Fig. 4**). Refraction disorder risk was linked to myopic features, including a significantly brighter fundus and an atrophic-appearing, thinner retina (**Fig. 2e, Supplementary Fig. 5**). Along the cataract risk

axis, images appeared greyer with reduced fundus visibility and subtle vessel thinning, consistent with cataract-related media opacity[27] (**Fig. 2f**, **Supplementary Fig. 6**).

Together, these analyses show that REECAP embeddings improve disease risk prediction and enable biological interpretation through generative modeling, capturing morphological features aligned with aging and ocular pathology.

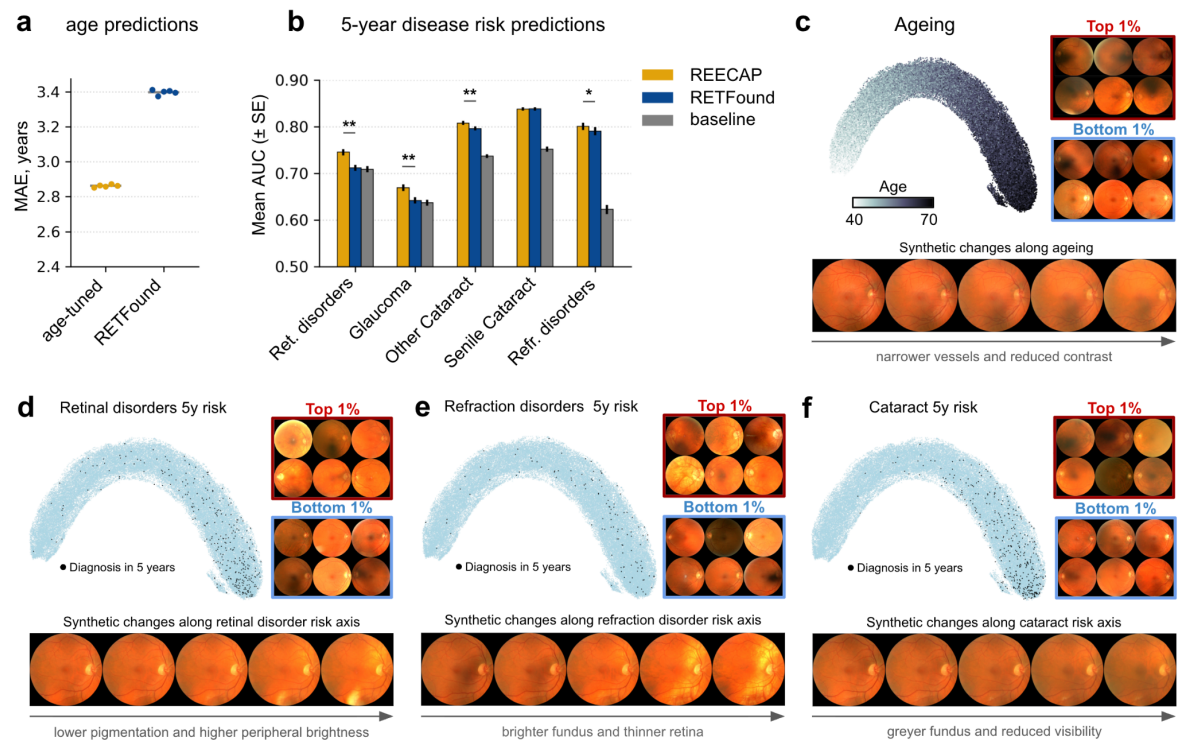

Figure 2 | REECAP embeddings improve age prediction and reveal disease-relevant retinal features. (**a**) Mean absolute error (MAE) for chronological age prediction using contrastively fine-tuned (REECAP) versus untuned RETFound embeddings. (**b**) Five-year disease risk prediction using ridge logistic regression trained on REECAP (gold), RETFound (blue), or scalar baseline features (gray). Bars show mean area under the ROC curve (AUC) across 20 random splits; *P < 0.05, **P < 0.0001 (paired t-test with Bonferroni correction). (**c**–**f**) Morphological variation along embedding-derived axes for (**c**) age, (**d**) retinal disorders (ICD10 H35), (**e**) refraction disorders (H52), and (**f**) cataracts (H25). Each panel shows a UMAP of REECAP embeddings colored by trait value, real fundus images from opposite ends of the axis, and synthetic images generated by a conditional generative model (**Methods**).

GWAS of REECAP embeddings identifies loci and pathways linked to eye aging and disease

To dissect the genetic architecture of eye aging captured by REECAP, we performed a multi-trait genome-wide association study (GWAS) using all embedding dimensions as a joint phenotype. The analysis included 36,349 unrelated European UKB participants with genotype

133 and high-quality imaging data. We adjusted for age, sex, and the top 20 genetic principal
134 components to account for population structure (**Methods**). Across 9,447,684 analyzed
135 common variants (minor allele frequency ≥1%), we identified 178 independent genome-wide
136 significant loci ($P < 5\times10^{-8}$; **Fig. 3a**, **Methods**), with well-calibrated test statistics under
137 permutation-based null models (**Supplementary Fig. 8**, **Methods**). This multivariate
138 approach nearly doubled the number of discovered loci compared to a univariate GWAS on
139 each embedding dimension with Cauchy-based P value aggregation[28] (178 vs. 90 loci;
140 **Supplementary Fig. 9**, **Methods**).
141
142 Colocalization with intermediate traits revealed that 41 of 178 loci (24%) overlap with retinal
143 vessel density[29] and 37 (21%) with hair color[30] (PP-H4 > 0.8; **Methods**, **Supplementary**
144 **Dataset 1**), highlighting vascular and pigmentation pathways as contributors to retinal aging.
145
146 Functional interpretation of common variant signals highlighted involved biological pathways.
147 MAGMA enrichment across 17,023 MSigDB gene sets revealed 5 significantly enriched
148 pathways (Bonferroni-adjusted $P < 2.94\times10^{-6}$, **Fig. 3b**, **Methods**), implicating pigmentation,
149 immune regulation, oxidative stress, and DNA damage responses as central processes in eye
150 aging. Additional non-significant enrichments pointed to synaptic plasticity and axon guidance,
151 consistent with neurodegenerative mechanisms in eye disease[31–33].
152
153 Tissue- and cell-type enrichment analyses based on common variant signals supported a
154 retinal origin for these signals, with the central retina emerging as the top-enriched tissue (**Fig.**
155 **3c**, **Methods**). Within the retina and macula, enrichment of genes mapped to the GWAS loci
156 was strongest in astrocytes, Müller cells, and retina pigment epithelium (RPE) (FDR < 5%,
157 **Fig. 3d**, **Methods**, **Supplementary Fig. 10**), while in the optic nerve head, astrocytes and
158 fibroblasts were also implicated (FDR < 5%), consistent with recent reports[34,35].
159
160 Integration with ocular disease GWAS in FinnGen revealed convergence with ocular disease.
161 Of the 178 loci, 27 (15.2%) colocalized with at least one eye disease (PP-H4 > 0.8, **Methods**),
162 including 14 loci not reaching genome-wide significance in FinnGen alone (**Fig. 3a**, black
163 stars; **Supplementary Dataset 1**). Colocalizations were most frequent with cataract, followed
164 by myopia, AMD, and glaucoma, with 9 loci colocalizing with more than one disease. In
165 comparison, the univariate GWAS yielded only 12 disease-colocalizing loci (**Methods**,
166 **Supplementary Fig. 11**).
167

Finally, applying the same multivariate framework to gene-level burden scores from rare coding variants in 17,984 genes within UKB revealed significant associations in melanin biosynthesis enzymes (*TYR*, *OCA2*, *SLC45A2*, *TYRP1*), visual cycle components (*RLBP1*, *RAB32*), and the matricellular protein *THBS4*, a regulator of vascular remodeling and age-related expression (**Supplementary Fig. 12**, **Methods**).

Collectively, these results position REECAP as a framework for linking image-derived phenotypes to genetic variation, revealing pathways and cell types relevant to eye aging and disease.

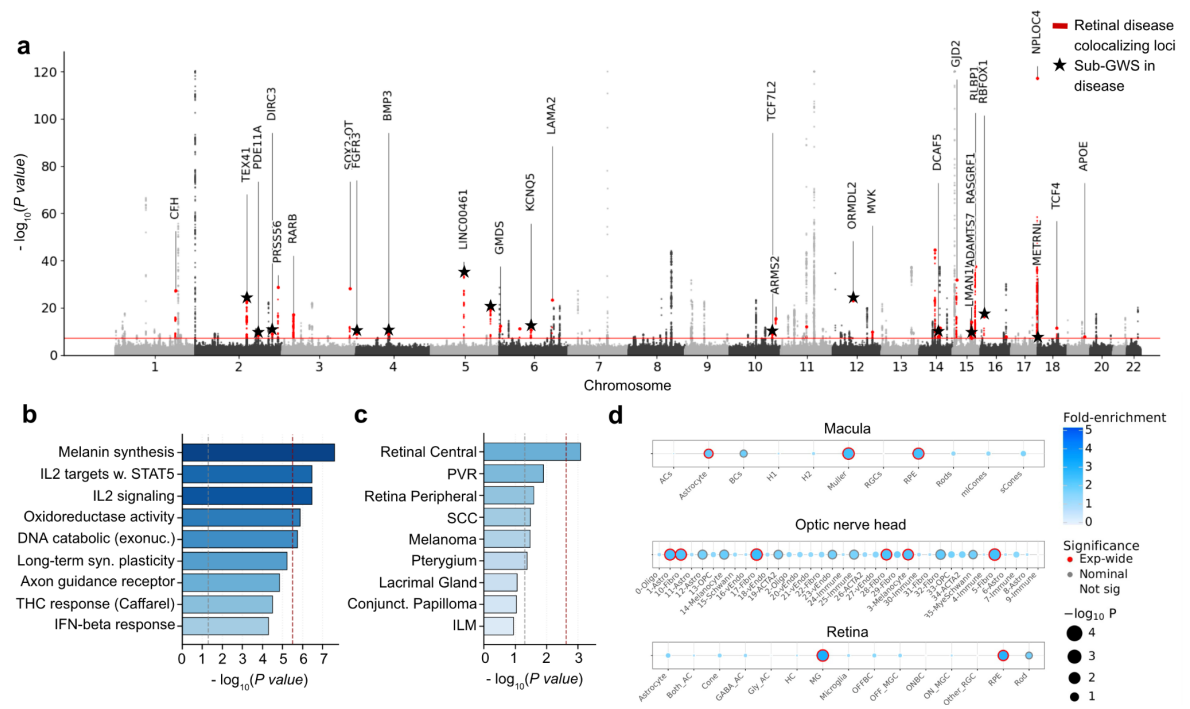

Figure 3 | Multi-trait GWAS of REECAP embeddings identifies loci, pathways, and cell types linked to retinal aging. (**a**) Manhattan plot of multi-trait GWAS of REECAP embeddings. Red points indicate loci colocalizing with ocular disease GWAS signals in FinnGen (PP-H4 > 0.8); black stars denote loci not genome-wide significant in FinnGen alone. Annotated genes mark closest genes to lead variants. (**b**) MAGMA gene-set enrichment highlights pigmentation, immune signaling, oxidative stress, and DNA damage response pathways. Bars show $-\log_{10}(P)$; red dashed line indicates Bonferroni threshold, black dashed line indicates nominal $P = 0.05$. Colors represent biological categories. (**c**) MAGMA tissue enrichment identifies the central retina as the top enriched tissue. Bars represent $-\log_{10}(P)$; significance thresholds as in **b**. (**d**) ECLIPSER analysis of cell-type enrichment in single-nucleus RNA-seq from three ocular tissues. Bubble size reflects $-\log_{10}(P)$, color denotes fold enrichment, and border shading indicates significant enrichments (5% FDR).

REECAP enhances genetic discovery and disease relevance over baseline models

To assess whether REECAP embeddings provided more informative genetic signals than other image-derived phenotypes, we benchmarked them against alternative representations: embeddings from the untuned RETFound encoder, embeddings from a domain-agnostic ResNet50 model (as in transferGWAS[36]), a scalar retinal age predictor, and the canonical imaging trait cup-to-disc ratio. We compared each method on the number of loci discovered, colocalization with disease GWAS, polygenic risk prediction, and pathway enrichment.

REECAP embeddings identified the largest number of independent genome-wide significant loci (178) and disease colocalizations (27), outperforming untuned RETFound (164 loci, 23 colocalizing), ImageNet-ResNet50 (94, 11), cup-to-disc ratio (26, 5), and scalar retinal age (6, 1) (**Fig. 4a–b, Methods**, **Supplementary Fig. 9**, **11**, **13**). Genetic risk scores derived from genome-wide significant loci were trained and validated on multiple UK Biobank train/test splits, with REECAP-based scores consistently outperforming baseline models in disease prediction accuracy (**Fig. 4c**; **Methods**).

Pathway analyses confirmed the disease relevance of REECAP signals. Although REECAP and RETFound embeddings exhibited similar heritability (**Methods**, **Supplementary Fig. 14**), REECAP prioritized pathways central to retinal biology, including melanin biosynthesis, *IL-2/STAT5* signaling, and oxidoreductase activity, while deprioritizing oxidoreductase and DNA catabolic programs strongly enriched in RETFound embeddings (**Fig. 4d**). In contrast, ImageNet-ResNet50 signals were enriched for more generic transcriptional pathways with limited connection to ocular aging (**Supplementary Dataset 2**).

Together, these findings show that REECAP embeddings yield genetic signals with stronger biological and disease relevance than either generic, unsupervised, or expert-defined image features, establishing fine-tuned representation learning as a powerful strategy for image–genomic phenotyping.

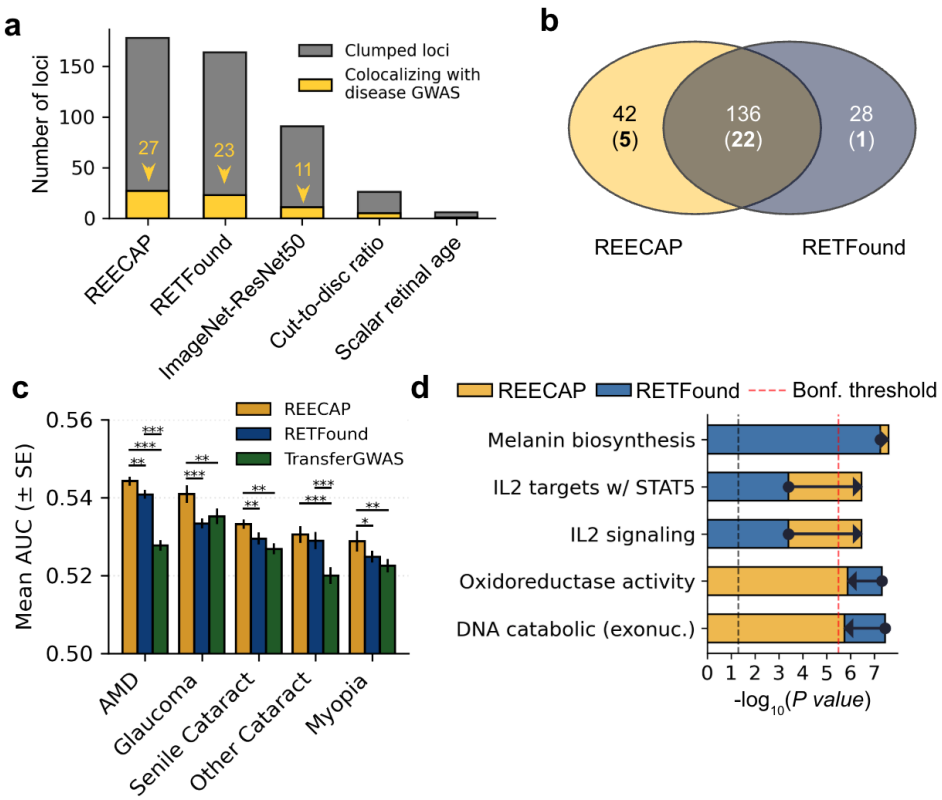

Figure 4 | REECAP embeddings outperform baseline image-derived phenotypes across genetic and disease-relevance benchmarks. (**a**) Number of independent genome-wide significant loci (gray) and disease GWAS colocalizations (PP-H4 > 0.80; yellow) identified using five imaging-derived traits: REECAP, RETFound, ImageNet-ResNet50, cup-to-disc ratio, and scalar retinal age. (**b**) Overlap between loci detected using REECAP versus RETFound embeddings; numbers in parentheses indicate loci colocalizing with disease GWAS. (**c**) Mean area under the ROC curve (AUC ± s.e.m.) for polygenic risk score (PRS) models of five ocular diseases, constructed using independent variants from each embedding type. *P < 0.05, **P < 0.01, ***P < 0.001 (paired t-test, N = 10). (**d**) MAGMA pathway enrichment ($-\log_{10}$P) for REECAP (yellow) versus RETFound (blue) across selected MSigDB gene sets. Arrows indicate differences between models. Red and black dashed lines denote Bonferroni and nominal significance thresholds, respectively.

Biological interpretation of REECAP loci across morphology and function

Among the 27 loci colocalizing with ocular disease, 13 mapped to well-established risk regions, providing biological validation of the REECAP approach. At *CFH*, the intronic variant *rs10737680* (P-REECAP < 10^{-25}) colocalized with four disease outcomes, including AMD and cataract (**Supplementary Dataset 1**), consistent with *CFH* role as a regulator of the complement cascade in retinal inflammation and aging[37–46]. Similarly, *rs3750846* at the *ARMS2–HTRA1* locus (P-REECAP < 10^{-15}) colocalized with all analyzed FinnGen eye outcomes (**Fig. 5a**, **Supplementary Dataset 1**) and has been extensively linked to AMD[47–55]. Synthetic image reconstruction revealed progressive fundus hypopigmentation along the risk

allele trajectory (**Fig. 5a**), consistent with early retinal pigment epithelium (RPE) thinning and melanin loss.

Beyond these established loci, REECAP uncovered 14 additional colocalizations not detected at genome-wide significance in disease-specific GWAS. Several signals reinforced prior links to ocular health: association signals at *KCNQ5* colocalized with myopia ($P < 10^{-10}$; PP-H4=0.996; **Supplementary Fig. 15**) and have been implicated in refractive error[56]; *BMP3* signals colocalized with retinal detachment (P-REECAP $< 10^{-8}$; PP-H4=0.906; **Supplementary Fig. 15**), consistent with previous evidence[57]; and a locus in *TCF7L2*, widely associated with diabetes[58–60], colocalized here with retinal disorders, including diabetic retinopathy (P-REECAP $< 10^{-8}$; PP-H4=0.993; **Supplementary Fig. 15**). A locus near *FGFR3* colocalized with cataract, in line with *FGFR3*'s established role in cataractogenesis[61,62].

REECAP additionally revealed loci with limited prior evidence linking them to ocular phenotypes. At *PDE11A*, the missense variant *rs17400325* (*Y727C,* P-REECAP $< 3\times10^{-9}$) colocalized with myopia in FinnGen (PP-H4 = 0.999; **Fig. 5b**) despite not reaching genome-wide significance there. Rare-variant analyses have previously implicated *PDE11A* in refractive error and myopia[63,64], and conditional image generation linked the risk allele to a brighter fundus and foveal greying, consistent with choroidal thinning in myopic remodeling[65]. Similarly, variant *rs7144307* in *DCAF5* (P-REECAP $< 1.2\times10^{-8}$) strongly colocalized with glaucoma (PP-H4 = 0.923; **Fig. 5c**) despite being subsignificant in the disease-label GWAS. *DCAF5* is expressed in the RPE, microglia, and optic nerve[66], and while conditional image generation suggested only subtle reduction in retinal pigmentation (**Fig. 5c**), knockout mice (*Dcaf5*$^{em1(IMPC)Ccpcz}$ allele) display abnormal retinal morphology, including dysplasia and retinal thinning, supporting a role in retinal homeostasis[67]. Other loci with moderate prior links to eye disease included variants in *RBFOX1, TEX41, LINC00461, ORDML2,* and *METRNL* (**Supplementary Fig. 15**).

Together, these analyses show that REECAP identifies both established and previously overlooked genetic associations and provides biological interpretation by linking risk variants to disease associations and retinal morphology.

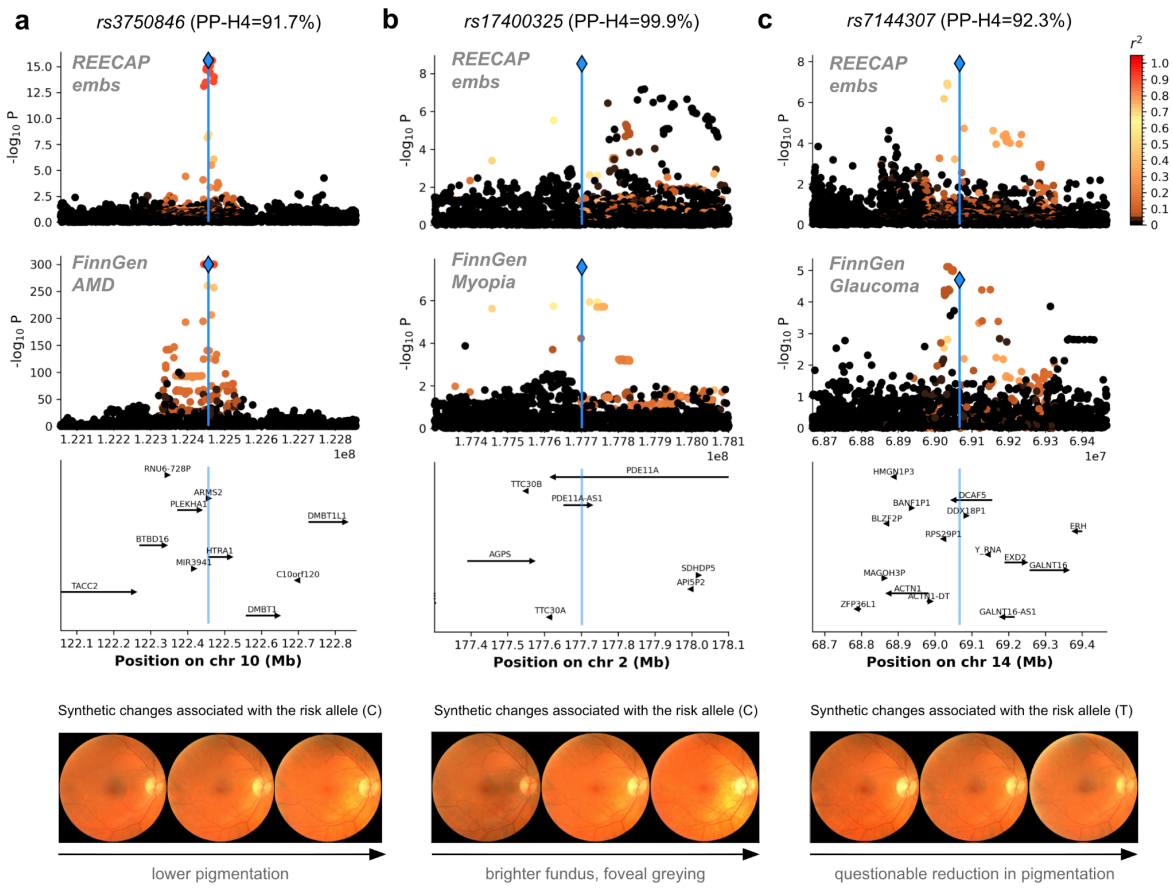

Figure 5 | Genetic loci identified by REECAP colocalize with ocular disease and enable morphological interpretation. (**a**–**c**) Representative loci colocalizing with ocular disease in FinnGen: *rs3750846* (*HTRA1–ARMS2*), *rs17400325* (*PDE11A*), and *rs7144307* (*DCAF5*). For each locus, shown are: (i) locus-specific Manhattan plot from the REECAP multi-trait GWAS, (ii) corresponding association signal from the FinnGen disease GWAS, (iii) gene annotations across the region, and (iv) synthetic fundus images generated by a conditional generative network, illustrating predicted morphological changes associated with the risk allele. Risk alleles are defined based on FinnGen disease associations (**Methods**).

Discussion

We introduce REECAP, an age-guided contrastive learning framework that fine-tunes vision foundation models to generate tissue ageing representations for genetic discovery, extending current univariate approaches to study tissue aging[68–70]. Applied to 87,478 fundus images from 52,742 individuals in the UK Biobank, REECAP identified 178 genome-wide significant loci, 68 of which (38%) colocalized with vessel density and pigmentation traits, supporting vascular and melanocytic changes as hallmarks of retinal aging. Enrichment analyses further implicated oxidative stress, immune regulation, and DNA damage pathways, with retinal glia and pigment epithelium emerging as key cellular contributors.

Beyond locus discovery, REECAP genetic signals act as priors for disease genetics, with 27 of the 178 loci colocalizing with major age-related eye diseases, including 14 missed by conventional disease-label GWAS. To visualize morphological changes associated with risk alleles, we used a conditional generative approach to synthesize fundus images along embedding-derived axes, which we validated on aging and disease-risk trajectories. We applied this framework to risk alleles at both known and novel loci, extending recent generative approaches for modeling genetic and chemical perturbations[12,71,72].

In a systematic genetics-centered comparison, we show that REECAP outperforms untuned foundation models, domain-agnostic embeddings, and expert-defined features across locus discovery, disease colocalization, and risk prediction. These findings suggest that REECAP can provide a general strategy for tuning vision foundation models for genetic analysis, offering a blueprint for applications to other tissues, modalities, and biological contexts.

REECAP recapitulated key loci involved in retinal aging and disease, including *CFH* and *ARMS2–HTRA1*, supporting its biological validity. It also uncovered novel associations: a missense variant in *PDE11A* (*rs17400325*) colocalized with myopia risk, consistent with rare-variant studies of refractive error[63,64]. Another locus, *DCAF5*, colocalized with glaucoma despite no prior human association; functional support from mouse knockout models showing retinal abnormalities[67], together with its role in the CUL4–DDB1 ubiquitin ligase complex[73], implicates *DCAF5* in retinal proteostasis and aging.

Several limitations warrant consideration. The genetic analyses were limited to individuals of European ancestry, and extending REECAP to more diverse populations will be essential for equitable genetic discovery. While REECAP embeddings capture aging-related variation, they are not explicitly tuned to disease-specific axes, which may be addressed in future domain-adaptive extensions. Finally, although generative reconstructions offer biologically plausible interpretations, empirical validation in model systems such as retinal organoids, animal knockouts, or longitudinal imaging will be necessary to confirm anatomical fidelity.

Together, these findings establish REECAP as a generalizable strategy for tuning vision foundation models for genetic analyses. By linking high-dimensional image features to genetic architecture and back to interpretable anatomy, REECAP advances the resolution, interpretability, and translational potential of imaging-genetic studies and offers a blueprint for foundation model alignment in diverse biomedical domains.

Methods

Data and Preprocessing

We analyzed genetic data and fundus photographs from the first imaging visit of 52,742 UK Biobank (UKB) participants[74]. High-quality images were identified using the MCF-Net model, retaining 87,478 images with a rejection probability below 80%[75]. Genetic analyses were conducted in 36,349 unrelated individuals of European ancestry[76]. Chronological age was obtained from UKB field 21003, and ICD-10 diagnosis codes were derived from hospital records, general practitioner reports, and self-reported data. Eye-related conditions were mapped using UKB category 2407.

The REECAP framework

REECAP is a representation learning framework that fine-tunes a foundation vision model to capture age-related morphological variation and trains a generative decoder to invert this embedding space, enabling direct visualization of changes along axes defined by traits or genetic variation. This joint architecture supports both statistical association analyses and interpretable image synthesis. In this study, we applied REECAP to retinal aging, initializing the model with the RETFound encoder, a ViT-large transformer pretrained for fundus image reconstruction[20,77].

Contrastive learning of aging. To align embeddings with continuous biological variation, we fine-tuned the RETFound encoder using Rank-N-Contrast (RnC), a contrastive learning framework optimized for regression tasks[22]. RnC organizes the latent space by enforcing ordinal relationships among samples within a batch: for each image, the model is trained to identify, among all younger samples, the one whose representation is closest to the focal point in latent space (**Supplementary Information**). This optimization encourages local ordering in accordance with chronological age, thereby structuring embeddings along the aging trajectory. Compared to direct regression losses, this approach yields more biologically informative representations and improves downstream age prediction[22]. We fine-tuned the RETFound model using images from both eyes, ensuring that images from the same participant were assigned to the same split. We evaluated performance via five-fold cross-validation, allocating 72% of the data for training, 8% for early stopping and augmentation selection, and 20% for testing (**Supplementary Fig. 16**). Training was performed using the AdamW optimizer[78] (learning rate = 5×10^{-6}; weight decay = 1×10^{-5}) with a batch size of 64.

Embedding definition. REECAP embeddings were obtained by averaging the 1,024-dimensional output of the fine-tuned RETFound encoder from left and right eye, followed by principal component analysis for dimensionality reduction prior to GWAS and visualization. For computational tractability, we retained the top 40 components, a number consistent with prior multivariate GWAS applications[8,12]. For visualization, UMAP was applied to a k-nearest neighbor graph (k = 10) using the `scanpy` package[79].

Generative decoder. To visualize the image-level information encoded by REECAP embeddings, we trained a conditional generative adversarial network (GAN) to synthesize fundus images from the 40-dimensional embeddings following the architecture in HistoGWAS[12]. The generator maps a latent variable **z**, sampled from a normal distribution whose mean and variance are functions of the REECAP embeddings **x**, to a 256 × 256 fundus image. The discriminator receives the embedding together with either a real or a synthetic image and is trained to distinguish between using a combination of conditional and unconditional adversarial losses, within a Wasserstein GAN framework with gradient penalty[80,81]. We also employed progressive growing of both generator and discriminator to enhance stability and image quality[82]. Architectural and training hyperparameters were aligned with those used in HistoGWAS[12] (**Supplementary Fig. 17**).

Conditional image generation. To visualize morphological changes associated with age, disease status, and genetic variation, we used the trained generative model to synthesize fundus images across relevant embedding trajectories[12]. For each trait of interest, we fitted a linear mixed model with the trait as the outcome, REECAP embeddings as random effects, and age, sex, and the top 20 genetic principal components as fixed effects. Leave-one-out (LOO) predictions of the random effect were computed for each individual[83], and mean embeddings were derived for individuals in the bottom and top 0.1% of the predicted distribution, denoted x_{low} and x_{high}, respectively. We then defined interpolated embeddings as:

$$x(\alpha) = (1-\alpha)\, x_{low} + \alpha\, x_{high}, \text{ for } \alpha \text{ in the range } [0,1],$$

and projected these embeddings back to image space using the GAN generator, enabling visual inspection of morphological changes along the interpolation axis. Multiple synthetic images can be generated for the same interpolated embeddings by sampling distinct latent noise vectors. The full procedure is detailed in **Supplementary Information**.

Validation of REECAP Embeddings

Age prediction performance. We benchmarked the predictive accuracy of REECAP embeddings against both untuned RETFound representations and supervised fine-tuning using a five-fold cross-validation framework. For REECAP and RETFound, ridge regression models with internal cross-validation for hyperparameter tuning were trained to predict chronological age from the corresponding representations. For the supervised baseline, we appended an average pooling layer and a linear output layer to the RETFound encoder and fine-tuned the model end-to-end using mean squared error loss. Training involved 15 warm-up epochs for the linear head (learning rate = 10^{-2}), followed by full model optimization at a reduced learning rate (10^{-6}). Prediction accuracy was evaluated using mean absolute error (MAE) between predicted and actual age in the held-out folds.

Disease risk prediction. We compared the ability of REECAP and untuned RETFound embeddings to predict five-year risk of major ocular diseases. ICD-10 diagnosis codes included other retinal diseases (H35; including age-related macular degeneration), glaucoma (H40), senile cataract (H25), other cataract (H26), and refraction disorders (H52; including myopia). For each method, the top 40 principal components of the representations were used as input features. To benchmark performance, we trained ridge logistic regression models using either REECAP or RETFound embeddings. As an additional baseline, we also evaluated a model using only demographic covariates: age, sex, age^2, sex × age, and sex × age^2. Predictive accuracy was measured using area under the receiver operating characteristic curve (AUC), averaged over 20 random 80/20 train–test splits, with five-fold cross-validation in each training set for hyperparameter tuning. Statistical significance of pairwise performance differences was assessed using paired t-tests across the test sets.

Visualization of ageing- and disease-associated changes. To assess whether REECAP embeddings capture meaningful morphological variation, we applied the conditional image generation described above to the following traits: age, retinal disorders, including AMD (ICD10 code H35: “other retinal diseases”), cataract (ICD10 code H25), and refraction disorders, including myopia (ICD10 code H52: “disorders of refraction and accommodation“). For each trait, synthetic images were generated by decoding interpolated embeddings along the corresponding direction. Multiple image realizations were produced per interpolation step by sampling different noise vectors. Two ophthalmologists reviewed the generated image sequences along each interpolation and documented characteristic morphological changes.

Genetic analysis of REECAP embeddings

Multi-trait GWAS. To identify genetic associations with REECAP embeddings, we performed a multi-trait genome-wide association study (MT-GWAS) using a re-implementation of the single-variant model described in [84]. Each embedding vector was modeled as a multivariate phenotype, and genetic effects were tested using a chi-squared statistic with 40 degrees of freedom. Residual trait covariance was estimated once under the null model and only partially optimized under the alternative for faster computation[84–86]. Full model details are provided in the **Supplementary Information**. GWAS was conducted in 36,349 unrelated individuals of European ancestry, testing 9,447,684 variants with minor allele frequency (MAF) ≥ 1%. Covariates included genotyping array, assessment center, age, sex, age^2, sex × age, sex × age^2, and the top 20 genetic principal components. Embedding dimensions were rank-normalized to standard Gaussian distributions to mitigate model mismatch due to deviation from Gaussian distribution. As a baseline, we also performed a univariate GWAS by testing each embedding dimension independently and combining P values using the aggregated Cauchy association test[28].

Independent genome-wide loci and colocalization. Independent genome-wide significant loci ($P < 5 \times 10^{-8}$) were identified using PLINK's clumping procedure[87] with an LD threshold of $r^2 < 0.1$ and a 5 Mb window. For each locus, we assessed overlap with disease-associated signals from genome-wide association studies of 10 ocular traits, using summary statistics from FinnGen (**Supplementary Information**). Loci that were genome-wide significant in the REECAP GWAS and associated with at least one ocular trait at a Bonferroni-adjusted $P < 0.05$ were tested for colocalization using the COLOC method[88]. We additionally evaluated colocalization with GWAS summary statistics for arterial vascular density[29] and hair color traits[30] (**Supplementary Information**).

Pathway Enrichment Analysis. To interpret biological pathways enriched in the multi-trait GWAS results, we used FUMA with integrated MAGMA[89] to perform gene-set enrichment analysis under default settings. Variant-level genome-wide association statistics were mapped to genes using MAGMA's SNP-wise mean model, with a default 0 kb SNP-to-gene window and LD estimated from the European 1000 Genomes Phase 3 reference panel. Enrichment was tested using MAGMA's competitive model, controlling for gene size, variant density, and LD structure, and evaluated against predefined gene sets from Gene Ontology and curated MSigDB pathways (v2023.1.Hs). We tested a total of 17,023 gene sets, and assessed significance after Bonferroni correction ($P < 2.94 \times 10^{-6}$).

Tissue and cell-type enrichment analyses. For tissue enrichment, we used MAGMA v1.10[89]. Transcriptomic data were obtained from the Human Eye Transcriptome Atlas[66], which includes gene expression profiles from multiple healthy and diseased eye tissues. Differential expression analysis was used to compute tissue specificity, and the top 10% of genes with the highest tissue-specific t-statistics were selected for each tissue[90]. These were tested for the tissue enrichment using MAGMA's competitive gene set analysis. Cell type enrichment was performed using ECLIPSER[34], applied to the 178 genome-wide significant loci identified in the REECAP GWAS.

Rare variant association testing. To identify associations between rare coding variants and REECAP embeddings, we computed DeepRVAT[91] burden scores from exome sequencing data for UKB individuals. We used the same multivariate linear model framework as in the multi-trait GWAS, but testing individual gene-level burden scores rather than individual variants. In total, we assessed 17,984 protein-coding genes.

Comparison to alternative methods

GWAS and colocalization benchmark. We compared multi-trait GWAS (MT-GWAS) discovery using REECAP embeddings to two baseline embeddings: untuned RETFound and ImageNet-pretrained ResNet-50 features, following the TransferGWAS framework[8]. For each method, the first 40 principal components (PCs) were taken as multivariate phenotypes in MT-GWAS. Scalar baselines included cup-to-disc ratio (UKB fields 27857 and 27858) and predicted age, the latter obtained from REECAP embeddings via elastic net leave-one-out cross-validation. Both scalar traits were analyzed using standard single-trait GWAS. All methods were applied to the same subset of UKB fundus images, with left and right eye representations averaged when available. For each method, we identified independent genome-wide significant loci using PLINK clumping ($r^2 < 0.1$, 5 Mb window, $P < 5 \times 10^{-8}$) and assessed colocalization with ocular disease GWAS from FinnGen using COLOC, as described above.

Heritability assessment. SNP-based heritability was estimated for all phenotypes using LD score regression (LDSC)[92]. GWAS summary statistics were first harmonized to HapMap3 variants using `munge_sumstats.py`, then analyzed with `ldsc.py --h2`, using chi-square statistics as the outcome. The analysis employed baselineLD v2.3 LD scores and the corresponding HapMap3 regression weights (`weights_hm3_no_hla`), thereby excluding the extended MHC region and adjusting for broad functional architecture, as recommended by the

baseline framework[93,94]. SNP heritability was reported on the observed scale, with standard errors estimated via block jackknife.

Polygenic risk score evaluation. We evaluated PRS performance for ocular diseases using genome-wide significant loci ($P < 5 \times 10^{-8}$) identified via multi-trait GWAS based on REECAP, untuned RETFound, or ImageNet-pretrained ResNet-50 embeddings. Independent variants were selected using LD-based clumping ($r^2 < 0.1$, 5 Mb window). Across 20 random 80/20 train/test splits in unrelated UK Biobank participants of European ancestry, we fitted logistic regression models in the training set to predict ICD-10–based ocular disease status (any-time diagnosis) and evaluated AUC in the test set. Method differences were assessed using paired t-tests.

Declarations

Competing interests

The authors declare that they have no competing interests.

Use of Artificial Intelligence

In the preparation of this manuscript, we utilized the large language model GPT-4 (https://chat.openai.com/) for editing assistance, including language polishing and clarification of text. While this tool assisted in refining the manuscript's language, it was not used to generate contributions to the original research, data analysis, or interpretation of results. All final content decisions and responsibilities rest with the authors.

Acknowledgements

We thank Dr. Khalid Aliyev for assistance with the annotation of the reconstructed images, and Brian Clarke for sharing variant annotations used for burden score computations. This research was conducted using the UK Biobank Resource (Application 87065). L.S., E.S., and B.E. were funded by Friedrich-Alexander-University Erlangen-Nuremberg. F.P.C., D.S., and S.C. were funded by the Free State of Bavaria's High-Tech Agenda through the Institute of AI for Health (AIH). L.S., D.S., and S.C. acknowledge support from HIDSS-006 – Munich School for Data Science@Helmholtz, TUM & LMU. A.V.S. and Q.X. were funded by NIH/NHLBI U01HL166060, and A.V.S. was also supported by NIH/NEI R01 EY031424. J.A.S. acknowledges funding from the Munich Center for Machine Learning (MCML) and the DAAD

program Konrad Zuse School of Excellence in Reliable Artificial Intelligence, sponsored by the German Federal Ministry of Research, Technology and Space (BMFTR).

Authors' contributions

L.S. implemented the methods and performed the main analyses. D.S., A.A., S.C., and Q.X. contributed to method development and data analysis. A.V.S., J.A.S., E.Sal., and N.C. provided critical guidance on study design, deep learning methodology, and result interpretation. J.S. and B.A. contributed ophthalmological expertise and provided clinical interpretation. O.V.A. and E.Sch. contributed to the integration of mouse clinic resources into the study. L.S. and F.P.C. wrote the manuscript with input from all authors. F.P.C. conceived the project with support from B.E.. F.P.C. and B.E. supervised the study.

References

1. Ji, Y. *et al.* Genome-Wide and Abdominal MRI Data Provide Evidence That a Genetically Determined Favorable Adiposity Phenotype Is Characterized by Lower Ectopic Liver Fat and Lower Risk of Type 2 Diabetes, Heart Disease, and Hypertension. *Diabetes* **68**, 207–219 (2018).
2. Agrawal, S. *et al.* Inherited basis of visceral, abdominal subcutaneous and gluteofemoral fat depots. *Nat. Commun.* **13**, 3771 (2022).
3. Meyer, H. V. *et al.* Genetic and functional insights into the fractal structure of the heart. *Nature* **584**, 589–594 (2020).
4. Smith, S. M. *et al.* An expanded set of genome-wide association studies of brain imaging phenotypes in UK Biobank. *Nat. Neurosci.* **24**, 737–745 (2021).
5. Elliott, L. T. *et al.* Genome-wide association studies of brain imaging phenotypes in UK Biobank. *Nature* **562**, 210–216 (2018).
6. Somineni, H. *et al.* Machine learning across multiple imaging and biomarker modalities in the UK Biobank improves genetic discovery for liver fat accumulation. *medRxiv* 2024.01.06.24300923 (2024) doi:10.1101/2024.01.06.24300923.
7. Liu, Y. *et al.* Genetic architecture of 11 organ traits derived from abdominal MRI using deep learning. *Elife* **10**, (2021).
8. Kirchler, M. *et al.* transferGWAS: GWAS of images using deep transfer learning. *Bioinformatics* **38**, 3621–3628 (2022).
9. Sergouniotis, P. I., Diakite, A., Gaurav, K., Birney, E. & Fitzgerald, T. Autoencoder-based phenotyping of ophthalmic images highlights genetic loci influencing retinal morphology and provides epidemiologically informative biomarkers. *bioRxiv* (2023)

505 doi:10.1101/2023.06.15.23291410.
506 10. Xie, Z. *et al.* iGWAS: Image-based genome-wide association of self-supervised deep
507 phenotyping of retina fundus images. *PLoS Genet.* **20**, e1011273 (2024).
508 11. Rakowski, A., Monti, R. & Lippert, C. TransferGWAS of T1-weighted brain MRI data from
509 UK Biobank. *PLoS Genet.* **20**, e1011332 (2024).
510 12. Chaudhary, S. *et al.* HistoGWAS: An AI-enabled Framework for Automated Genetic
511 Analysis of Tissue Phenotypes in Histology Cohorts. *bioRxiv* 2024–2006 (2024).
512 13. Xu, W. *et al.* Deep learning and genome-wide association meta-analyses of bone marrow
513 adiposity in the UK Biobank. *Nat. Commun.* **16**, 99 (2025).
514 14. Paschali, M. *et al.* Foundation models in radiology: What, how, why, and why not.
515 *Radiology* **314**, e240597 (2025).
516 15. Moor, M. *et al.* Foundation models for generalist medical artificial intelligence. *Nature* **616**,
517 259–265 (2023).
518 16. Chen, R. J. *et al.* Towards a general-purpose foundation model for computational
519 pathology. *Nat. Med.* **30**, 850–862 (2024).
520 17. Lu, M. Y. *et al.* A visual-language foundation model for computational pathology. *Nat.*
521 *Med.* **30**, 863–874 (2024).
522 18. Yan, S. *et al.* A multimodal vision foundation model for clinical dermatology. *Nat. Med.*
523 **31**, 2691–2702 (2025).
524 19. Pai, S. *et al.* Foundation model for cancer imaging biomarkers. *Nat. Mach. Intell.* **6**, 354–
525 367 (2024).
526 20. Zhou, Y. *et al.* A foundation model for generalizable disease detection from retinal images.
527 *Nature* **622**, 156–163 (2023).
528 21. Zhang, J. *et al.* RETFound-enhanced community-based fundus disease screening: real-
529 world evidence and decision curve analysis. *NPJ Digit. Med.* **7**, 108 (2024).
530 22. Zha, K., Cao, P., Son, J., Yang, Y. & Katabi, D. Rank-n-contrast: learning continuous
531 representations for regression. *Adv. Neural Inf. Process. Syst.* **36**, (2024).
532 23. Ege, B. M., Hejlesen, O. K., Larsen, O. V. & Bek, T. The relationship between age and
533 colour content in fundus images. *Acta Ophthalmol. Scand.* **80**, 485–489 (2002).
534 24. Bhatia, S. K. *et al.* Analysis of RPE morphometry in human eyes. *Mol. Vis.* **22**, 898 (2016).
535 25. Wong, T. Y., Klein, R., Klein, B. E. K., Meuer, S. M. & Hubbard, L. D. Retinal vessel
536 diameters and their associations with age and blood pressure. *Invest. Ophthalmol. Vis.*
537 *Sci.* **44**, 4644–4650 (2003).
538 26. Lee, J. *et al.* Pigmentary abnormality without significant drusen as a risk factor for late
539 age-related macular degeneration. *Sci. Rep.* **12**, 769 (2022).
540 27. Mai, E. L. C., Chen, B.-H. & Su, T.-Y. Innovative utilization of ultra-wide field fundus
541 images and deep learning algorithms for screening high-risk posterior polar cataract. *J.*

542 *Cataract Refract. Surg.* **50**, 618–623 (2024).
543 28. Liu, Y. *et al.* ACAT: a fast and powerful p value combination method for rare-variant
544 analysis in sequencing studies. *Am. J. Hum. Genet.* **104**, 410–421 (2019).
545 29. Ortín Vela, S. *et al.* Phenotypic and genetic characteristics of retinal vascular parameters
546 and their association with diseases. *Nat. Commun.* **15**, 9593 (2024).
547 30. Jiang, L., Zheng, Z., Fang, H. & Yang, J. A generalized linear mixed model association
548 tool for biobank-scale data. *Nat. Genet.* **53**, 1616–1621 (2021).
549 31. Narasimhan, A. *et al.* The Ercc1-/Δ mouse model of XFE progeroid syndrome undergoes
550 accelerated retinal degeneration. *Aging Cell* **24**, e14419 (2025).
551 32. Blasiak, J., Pawlowska, E., Sobczuk, A., Szczepanska, J. & Kaarniranta, K. The aging
552 stress response and its implication for AMD pathogenesis. *Int. J. Mol. Sci.* **21**, 8840
553 (2020).
554 33. Pauwels, L., Chalavi, S. & Swinnen, S. P. Aging and brain plasticity. *Aging (Albany NY)*
555 **10**, 1789–1790 (2018).
556 34. Hamel, A. R. *et al.* Integrating genetic regulation and single-cell expression with GWAS
557 prioritizes causal genes and cell types for glaucoma. *Nat. Commun.* **15**, 396 (2024).
558 35. Benhar, I. *et al.* Temporal single-cell atlas of non-neuronal retinal cells reveals dynamic,
559 coordinated multicellular responses to central nervous system injury. *Nat. Immunol.* **24**,
560 700–713 (2023).
561 36. Kirchler, M. *et al.* transferGWAS: GWAS of images using deep transfer learning.
562 *Bioinformatics* **38**, 3621–3628 (2022).
563 37. Goto, A. *et al.* Genetic analysis of typical wet-type age-related macular degeneration and
564 polypoidal choroidal vasculopathy in Japanese population. *J. Ocul. Biol. Dis. Infor.* **2**, 164–
565 175 (2009).
566 38. Chen, W. *et al.* Genetic variants near TIMP3 and high-density lipoprotein--associated loci
567 influence susceptibility to age-related macular degeneration. *Proceedings of the National*
568 *Academy of Sciences* **107**, 7401–7406 (2010).
569 39. Neale, B. M. *et al.* Genome-wide association study of advanced age-related macular
570 degeneration identifies a role of the hepatic lipase gene (LIPC). *Proceedings of the*
571 *National Academy of Sciences* **107**, 7395–7400 (2010).
572 40. Raychaudhuri, S. *et al.* A rare penetrant mutation in CFH confers high risk of age-related
573 macular degeneration. *Nat. Genet.* **43**, 1232–1236 (2011).
574 41. Raychaudhuri, S. *et al.* Associations of CFHR1--CFHR3 deletion and a CFH SNP to age-
575 related macular degeneration are not independent. *Nat. Genet.* **42**, 553–555 (2010).
576 42. Leveziel, N. *et al.* Genetic factors for choroidal neovascularization associated with high
577 myopia. *Invest. Ophthalmol. Vis. Sci.* **53**, 5004–5009 (2012).
578 43. Mandal, N. A. & Ayyagari, R. Complement factor H: spatial and temporal expression and

579 localization in the eye. *Invest. Ophthalmol. Vis. Sci.* **47**, 4091–4097 (2006).
580 44. Sivapathasuntharam, C. *et al.* Complement factor H regulates retinal development and
581 its absence may establish a footprint for age related macular degeneration. *Sci. Rep.* **9**,
582 1082 (2019).
583 45. Desai, D. & Dugel, P. U. Complement cascade inhibition in geographic atrophy: a review.
584 *Eye* **36**, 294–302 (2022).
585 46. Ding, J.-D. *et al.* Expression of human complement factor H prevents age-related macular
586 degeneration--like retina damage and kidney abnormalities in aged Cfh knockout mice.
587 *Am. J. Pathol.* **185**, 29–42 (2015).
588 47. Edwards, D. R. V. *et al.* Inverse association of female hormone replacement therapy with
589 age-related macular degeneration and interactions with ARMS2 polymorphisms. *Invest.*
590 *Ophthalmol. Vis. Sci.* **51**, 1873–1879 (2010).
591 48. Friedrich, U. *et al.* Risk-and non-risk-associated variants at the 10q26 AMD locus
592 influence ARMS2 mRNA expression but exclude pathogenic effects due to protein
593 deficiency. *Hum. Mol. Genet.* **20**, 1387–1399 (2011).
594 49. Fritsche, L. G. *et al.* A large genome-wide association study of age-related macular
595 degeneration highlights contributions of rare and common variants. *Nat. Genet.* **48**, 134–
596 143 (2016).
597 50. Farinha, C. *et al.* Common and rare genetic risk variants in age-related macular
598 degeneration and genetic risk score in the Coimbra eye study. *Acta Ophthalmol.* **101**,
599 185–199 (2023).
600 51. Huang, G. *et al.* Association analysis of seven single nucleotide polymorphisms identified
601 by genome-wide association study with age-related macular degeneration among ethnic
602 Han Chinese population. *Zhonghua Yi Xue Yi Chuan Xue Za Zhi* **39**, 963–968 (2022).
603 52. Sun, S. *et al.* Bringing the age-related macular degeneration high-risk allele age-related
604 maculopathy susceptibility 2 into focus with stem cell technology. *Stem Cell Research &*
605 *Therapy* **8**, 1–7 (2017).
606 53. Chakravarthy, U. *et al.* ARMS2 increases the risk of early and late age-related macular
607 degeneration in the European Eye Study. *Ophthalmology* **120**, 342–348 (2013).
608 54. Thee, E. F. *et al.* The phenotypic course of age-related macular degeneration for
609 ARMS2/HTRA1: the EYE-RISK consortium. *Ophthalmology* **129**, 752–764 (2022).
610 55. Mori, K. *et al.* Association of the HTRA1 gene variant with age-related macular
611 degeneration in the Japanese population. *J. Hum. Genet.* **52**, 636–641 (2007).
612 56. Liao, X. *et al.* Genetic association study of KCNQ5 polymorphisms with high myopia.
613 *Biomed Res. Int.* **2017**, 3024156 (2017).
614 57. Boutin, T. S. *et al.* Insights into the genetic basis of retinal detachment. *Hum. Mol. Genet.*
615 **29**, 689–702 (2020).

616 58. Palmer, N. D. *et al.* Resequencing and analysis of variation in the TCF7L2 gene in African
617 Americans suggests that SNP rs7903146 is the causal diabetes susceptibility variant.
618 *Diabetes* **60**, 662–668 (2011).
619 59. Ghassibe-Sabbagh, M. *et al.* T2DM GWAS in the Lebanese population confirms the role
620 of TCF7L2 and CDKAL1 in disease susceptibility. *Sci. Rep.* **4**, 7351 (2014).
621 60. Chang, S. *et al.* Association between TCF7L2 polymorphisms and gestational diabetes
622 mellitus: A meta-analysis. *J. Diabetes Investig.* **8**, 560–570 (2017).
623 61. Audette, D. S. *et al.* Prox1 and fibroblast growth factor receptors form a novel regulatory
624 loop controlling lens fiber differentiation and gene expression. *Development* **143**, 318–
625 328 (2016).
626 62. Zhao, H. *et al.* Fibroblast growth factor receptor signaling is essential for lens fiber cell
627 differentiation. *Dev. Biol.* **318**, 276–288 (2008).
628 63. Sbornova, I. *et al.* The sleep quality-and myopia-linked PDE11A-Y727C variant impacts
629 neural physiology by reducing catalytic activity and altering subcellular
630 compartmentalization of the enzyme. *Cells* **12**, 2839 (2023).
631 64. Guggenheim, J. A. *et al.* Whole exome sequence analysis in 51 624 participants identifies
632 novel genes and variants associated with refractive error and myopia. *Hum. Mol. Genet.*
633 **31**, 1909–1919 (2022).
634 65. Jonas, J. B., Ohno-Matsui, K. & Panda-Jonas, S. Myopia: Anatomic changes and
635 consequences for its etiology. *Asia Pac. J. Ophthalmol. (Phila.)* **8**, 355–359 (2019).
636 66. Wolf, J. *et al.* The Human Eye Transcriptome Atlas: A searchable comparative
637 transcriptome database for healthy and diseased human eye tissue. *Genomics* **114**,
638 110286 (2022).
639 67. Brown, S. D. M. & Moore, M. W. The International Mouse Phenotyping Consortium: past
640 and future perspectives on mouse phenotyping. *Mamm. Genome* **23**, 632–640 (2012).
641 68. Huang, Y. *et al.* Genomic determinants of biological age estimated by deep learning
642 applied to retinal images. *GeroScience* **47**, 2613–2629 (2025).
643 69. Ahadi, S. *et al.* Longitudinal fundus imaging and its genome-wide association analysis
644 provide evidence for a human retinal aging clock. *Elife* **12**, (2023).
645 70. Miao, H. *et al.* Artificial intelligence-derived retinal age gap as a marker for reproductive
646 aging in women. *NPJ Digit. Med.* **8**, 367 (2025).
647 71. Palma, A., Theis, F. J. & Lotfollahi, M. Predicting cell morphological responses to
648 perturbations using generative modeling. *Nat. Commun.* **16**, 505 (2025).
649 72. Lotfollahi, M. *et al.* Predicting cellular responses to complex perturbations in high-
650 throughput screens. *Mol. Syst. Biol.* **19**, e11517 (2023).
651 73. Radko-Juettner, S. *et al.* Targeting DCAF5 suppresses SMARCB1-mutant cancer by
652 stabilizing SWI/SNF. *Nature* **628**, 442–449 (2024).

74. Sudlow, C. *et al.* UK biobank: an open access resource for identifying the causes of a wide range of complex diseases of middle and old age. *PLoS Med.* **12**, e1001779 (2015).
75. Fu, H. *et al.* Evaluation of retinal image quality assessment networks in different color-spaces. in *Medical Image Computing and Computer Assisted Intervention--MICCAI 2019: 22nd International Conference, Shenzhen, China, October 13--17, 2019, Proceedings, Part I 22* 48–56 (Springer, 2019).
76. UK Biobank. *Genotyping and Quality Control in UK Biobank, Interim Release*. https://biobank.ctsu.ox.ac.uk/crystal/crystal/docs/genotyping_qc.pdf (2020).
77. He, K. *et al.* Masked autoencoders are scalable vision learners. in *Proceedings of the IEEE/CVF conference on computer vision and pattern recognition* 16000–16009 (2022).
78. Loshchilov, I. Decoupled weight decay regularization. *arXiv preprint arXiv:1711. 05101* (2017).
79. Wolf, F. A., Angerer, P. & Theis, F. J. SCANPY: large-scale single-cell gene expression data analysis. *Genome Biol.* **19**, 1–5 (2018).
80. Arjovsky, M., Chintala, S. & Bottou, L. Wasserstein generative adversarial networks. in *International conference on machine learning* 214–223 (PMLR, 2017).
81. Gulrajani, I., Ahmed, F., Arjovsky, M., Dumoulin, V. & Courville, A. C. Improved training of wasserstein gans. *Adv. Neural Inf. Process. Syst.* **30**, (2017).
82. Karras, T. Progressive Growing of GANs for Improved Quality, Stability, and Variation. *arXiv preprint arXiv:1710. 10196* (2017).
83. Mefford, J. *et al.* Efficient estimation and applications of cross-validated genetic predictions to polygenic risk scores and linear mixed models. *Journal of Computational Biology* **27**, 599–612 (2020).
84. Casale, F. P., Rakitsch, B., Lippert, C. & Stegle, O. Efficient set tests for the genetic analysis of correlated traits. *Nat. Methods* **12**, 755–758 (2015).
85. Lippert, C., Casale, F. P., Rakitsch, B. & Stegle, O. LIMIX: genetic analysis of multiple traits. *bioRxiv* 003905 (2014).
86. Korte, A. *et al.* A mixed-model approach for genome-wide association studies of correlated traits in structured populations. *Nat. Genet.* **44**, 1066–1071 (2012).
87. Purcell, S. *et al.* PLINK: a tool set for whole-genome association and population-based linkage analyses. *Am. J. Hum. Genet.* **81**, 559–575 (2007).
88. Giambartolomei, C. *et al.* Bayesian test for colocalisation between pairs of genetic association studies using summary statistics. *PLoS Genet.* **10**, e1004383 (2014).
89. de Leeuw, C. A., Mooij, J. M., Heskes, T. & Posthuma, D. MAGMA: generalized gene-set analysis of GWAS data. *PLoS Comput. Biol.* **11**, e1004219 (2015).
90. Finucane, H. K. *et al.* Heritability enrichment of specifically expressed genes identifies disease-relevant tissues and cell types. *Nat. Genet.* **50**, 621–629 (2018).

690 91. Clarke, B. *et al.* Integration of variant annotations using deep set networks boosts rare
691 variant association testing. *Nat. Genet.* **56**, 2271–2280 (2024).
692 92. Bulik-Sullivan, B. K. *et al.* LD Score regression distinguishes confounding from
693 polygenicity in genome-wide association studies. *Nat. Genet.* **47**, 291–295 (2015).
694 93. Finucane, H. K. *et al.* Partitioning heritability by functional annotation using genome-wide
695 association summary statistics. *Nat. Genet.* **47**, 1228–1235 (2015).
696 94. Gazal, S. *et al.* Linkage disequilibrium-dependent architecture of human complex traits
697 shows action of negative selection. *Nat. Genet.* **49**, 1421–1427 (2017).